

Shortwave infrared polymethine fluorophores matched to excitation lasers enable non-invasive, multicolour in vivo imaging in real time

Emily D. Cosco^{1,2}, Anthony L. Spearman¹, Shyam Ramakrishnan[©]², Jakob G. P. Lingg², Mara Saccomano², Monica Pengshung¹, Bernardo A. Arús[©]², Kelly C. Y. Wong[©]¹, Sarah Glasl³, Vasilis Ntziachristos[©]³, Martin Warmer², Ryan R. McLaughlin¹, Oliver T. Bruns[©]² and Ellen M. Sletten[©]¹

High-resolution, multiplexed experiments are a staple in cellular imaging. Analogous experiments in animals are challenging, however, due to substantial scattering and autofluorescence in tissue at visible (350-700 nm) and near-infrared (700-1,000 nm) wavelengths. Here, we enable real-time, non-invasive multicolour imaging experiments in animals through the design of optical contrast agents for the shortwave infrared (SWIR, 1,000-2,000 nm) region and complementary advances in imaging technologies. We developed tunable, SWIR-emissive flavylium polymethine dyes and established relationships between structure and photophysical properties for this class of bright SWIR contrast agents. In parallel, we designed an imaging system with variable near-infrared/SWIR excitation and single-channel detection, facilitating video-rate multicolour SWIR imaging for optically guided surgery and imaging of awake and moving mice with multiplexed detection. Optimized dyes matched to 980 nm and 1,064 nm lasers, combined with the clinically approved indocyanine green, enabled real-time, three-colour imaging with high temporal and spatial resolutions.

mprovements in imaging technologies and optical probes have combined to revolutionize our ability to study cells and small organisms using fluorescence microscopy^{1,2}. The tools developed for fluorescent imaging in cells can be readily applied to small model organisms such as Caenorhabditis elegans, Danio rerio (zebrafish) and Drosophila melanogaster. Translating these tools to mammals is challenging, however, as most fluorophores used in cellular imaging are excited by light in the visible (VIS, 350-700 nm) region of the electromagnetic spectrum, which exhibits low photon penetration and high background autofluorescence. For these reasons, imaging in mammals has been primarily focused on the near-infrared (NIR, 700-1,000 nm) region, where there are fewer endogenous chromophores, but where light scattering remains a limitation³. Further, the limited wavelength range of the NIR makes multiplexed experiments challenging. Notable approaches to multicolour fluorescence imaging experiments in mice that are compatible with VIS and NIR fluorophores include two-photon intravital microscopy methods, requiring body windows⁴⁻⁷, or endoscopy⁸. Efforts towards non-invasive, multiplexed imaging in mice have been explored with quantum dots9, fluorescently labelled silica particles10, fluorescent proteins¹¹ and surface-enhanced Raman scattering nanoparticles¹². While critical advances, these approaches suffer from low spatial and temporal resolution, limiting the biological information that can be obtained.

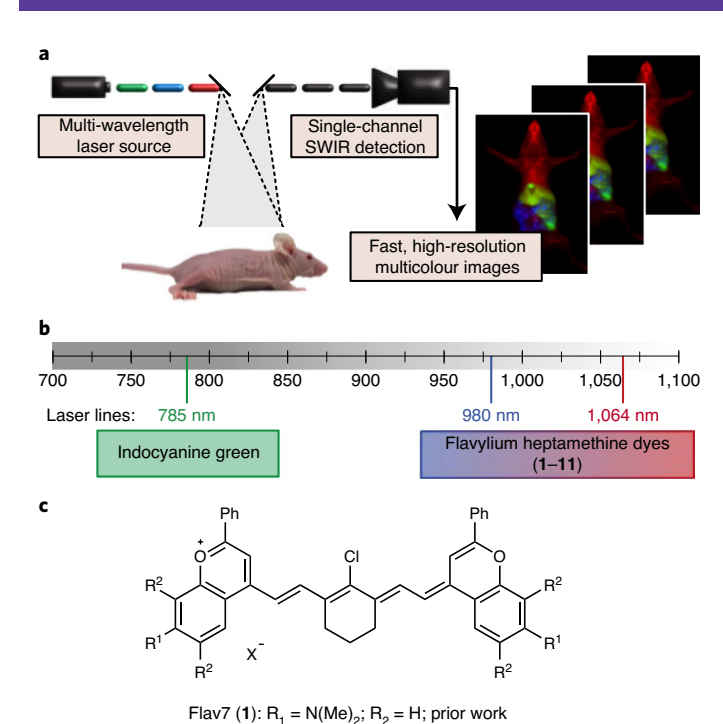
To enable robust, real-time, multiplexed imaging in animals it is necessary to (1) detect in a region of the electromagnetic spectrum that provides high spatial resolution; (2) establish efficient, orthogonal excitation and/or detection of bright fluorophores; and (3) rapidly

detect each channel on the millisecond timescale. Here, we present a method that meets these requirements and enables whole-animal, three-colour imaging with high spatial and temporal resolutions. Key to this technique is the implementation of excitation multiplexing and 'colour-blind' single-channel detection of low-energy shortwave infrared (SWIR, 1,000–2,000 nm) light emitted by bright, 'excitation-matched' polymethine fluorophores (Fig. 1a).

The SWIR region is essential for multiplexed in vivo fluorescence imaging, as it provides superior resolution and greater tissue penetration than the NIR region^{13,14} in addition to an expanded range of wavelengths allowing for multiple channels¹⁵ separated by at least 80 nm. The optimal properties of the SWIR for in vivo imaging were first demonstrated with carbon nanotubes¹⁶ and further validated with quantum dots^{17,18}, rare-earth nanomaterials¹⁵ and small molecules^{19,20}. Combinations of these materials have been utilized to obtain multiplexed images in mice^{18,21-23} and tissues²⁴ at higher spatial resolutions than NIR images. The approach of excitation multiplexing with single-channel SWIR detection reported herein addresses multicolour SWIR imaging with high temporal resolution, facilitating real-time analysis (>27 frames per second (fps)) of biological processes at sub-millimetre resolutions.

To facilitate rapid multicolour imaging in the SWIR region, we diverged from traditional multiplexing approaches employing a common excitation wavelength and different detection windows^{15,21–25} or spectral unmixing¹⁸. These classic approaches can result in different resolutions for each channel due to dramatic changes in the contrast and resolution that occur throughout wavelength bands of the NIR and SWIR^{14,26,27}. Furthermore, fast

¹Department of Chemistry and Biochemistry, University of California, Los Angeles, Los Angeles, CA, USA. ²Helmholtz Pioneer Campus, Helmholtz Zentrum München, Neuherberg, Germany. ³Institute of Biomedical Imaging, Helmholtz Zentrum München, Neuherberg, Germany. [™]e-mail: oliver.bruns@helmholtz-muenchen.de; sletten@chem.ucla.edu



2–11: R_1 = alkyl and aromatic amines, methoxy, H; R_2 = H, alkyl; this work

Fig. 1 | Real-time excitation-multiplexed SWIR imaging design.

a, Multiple laser sources are pulsed and delivered to the biological sample. Single-channel SWIR detection (InGaAs, 1,100-1,700 nm) acquires frames that are temporally separated by colour on the millisecond timescale. Fast frame rates produce real-time multicolour in vivo images at up to 50 fps.
b, Relevant portions of the NIR and SWIR regions of the electromagnetic spectrum, lasers used for excitation and dyes used and/or presented in this study that are excited by the distinct laser lines. c, Flavylium polymethine scaffold explored here to match bright SWIR dyes to appropriate lasers.

imaging speeds can be impeded by low photon throughput in sectioned regions of the electromagnetic spectrum or by mechanical components, such as filter wheels. Instead of these approaches, we differentiate the contrast agents via excitation wavelength and employ a single SWIR detection channel. This method, referred to as excitation multiplexing, is advantageous due to the consistent resolution achieved in all channels, high photon efficiency and ease of rapid collection of each frame on a single detector^{28,29}. Excitation multiplexing was initially applied to single-molecule spectroscopy methods, microscopy and low-concentration DNA sequencing³⁰. Subsequent variations on these methods have been explored^{31,32}, but excitation-multiplexed methods have yet to be adapted for animals. The implementation of excitation multiplexing in the SWIR is particularly beneficial as excitation can be optimized for each fluorophore and photons can be detected over a wide range of wavelengths. These properties combine to maximize the signal obtained from SWIR contrast agents, which have inherently low quantum yields when compared to those in the VIS and NIR³³.

To perform real-time excitation multiplexing in animals, bright SWIR-emissive contrast agents with absorption spectra compatible with common and cost-efficient laser lines are required (Fig. 1b). Polymethine dyes are opportune contrast agents for excitation multiplexing as they have characteristically narrow absorption bands with high absorption coefficients³⁴. A preeminent member of the polymethine dye family is indocyanine green (ICG), an FDA-approved contrast agent^{35,36}. While ICG has been extensively used in NIR optical imaging, in 2017, we reported that the dye can be detected readily in a SWIR imaging configuration due to the

long tail of the emission spectrum^{37,38}. Concurrently, we reported a polymethine dye designed for SWIR optical imaging³⁹. This dye, Flav7 (1, Fig. 1c), has both SWIR absorption and high brightness for the SWIR region. Notably, since the introduction of Flav7, similar strategies have been employed to utilize or design polymethine dyes for SWIR imaging⁴⁰⁻⁴⁴. Due to the ability to image both bright NIR-excitable dyes, such as ICG, as well as red-shifted SWIR-excitable polymethine dyes, such as Flav7, using an identical SWIR detection window, we envisioned that polymethine dyes with both well-separated and laser-line-compatible absorption could enable efficient multicolour SWIR imaging via excitation multiplexing. To realize this multiplexing strategy, structural modifications to Flav7 were necessary to tune the wavelength of maximum absorption ($\lambda_{\text{max,abs}}$) to match the accessible laser wavelengths used for SWIR imaging. Towards this goal, we set out to fine-tune the absorption properties of flavylium polymethine dyes through heterocycle modification. This work ultimately allowed access to a set of dyes that were optimal for real-time, multicolour SWIR imaging (see Fig. 2a).

Results

Design and synthesis of flavylium heptamethine dyes. To tune the absorption properties of flavylium polymethine dyes for excitation multiplexing, robust synthetic approaches towards flavylium heterocycles were necessary. The original report of Flav7 used a previously published⁴⁵, low-yielding, electronically sensitive and potentially explosive route. We developed an alternate approach relying on a key 7-substituted flavone intermediate that could be converted to the desired heterocycles by treatment with a methyl nucleophile and dehydration (Extended Data Fig. 1)46. Using three general routes to flavones, (1) Mentzer pyrone synthesis⁴⁷, (2) functionalization of 7-hydroxyflavone by Buchwald-Hartwig coupling of the corresponding triflate⁴⁸ and (3) acylation of the commercial 7-aminoflavone, we accessed a diverse set of 7-aminoflavylium heterocycles (Supplementary Tables 1-3). The heptamethine dyes 1-11 (Fig. 2a) were then obtained through the base-promoted reaction of each flavylium heterocycle with the relevant bis(phenylimine) polymethine chain (Supplementary Table 4; see Supplementary Note 1 for further discussion).

Photophysical characterization of flavylium heptamethine dyes.

Differences in $\lambda_{\text{max,abs}}$ are essential for excitation multiplexing. We characterized the photophysical properties of 1-11 in dichloromethane (DCM), finding that the flavylium heptamethine dyes have absorption/emission spanning the NIR to SWIR regions of the electromagnetic spectrum (Fig. 2a-c, Table 1). Compared to Flav7 (1), with $\lambda_{\text{max abs}} = 1,027 \,\text{nm}$, 9 and 10 underwent hypsochromic shifts. The 7-methoxy-substituted dye 10 is ~43 nm blue-shifted from Flav7 ($\lambda_{\text{max,abs}} = 984 \,\text{nm}$), similar to the unsubstituted flavylium dye 11 (IR-27)⁴⁹. Conversely, dyes 3 and 7 displayed substantial bathochromic shifts compared to Flav7. The diphenylamino-substituted 7 is ~23 nm red-shifted, while julolidine derivative 3 is red-shifted by $\sim 35 \,\text{nm}$ ($\lambda_{\text{max,abs}} = 1,061 \,\text{nm}$). Linear and cyclic aliphatic amine-substituted dyes 2 and 4-6 exhibit minor red-shifts. Plotting absorption/emission wavelengths of nine dyes in the series against Hammett $\sigma_{\rm m}$ values⁵⁰ resulted in a strong correlation ($R^2 = 0.96$; Fig. 2d and Supplementary Note 2). This increased understanding of the relationship between structure and absorption/emission wavelengths sets up opportunities for predicting fluorophore structures to match any desired excitation wavelength.

Further characterization of the panel of flavylium polymethine dyes was necessary to determine their maximum brightness (brightness(ε_{λ}) = $\varepsilon_{\lambda} \times \Phi_{\rm F}$). We found that the absorption coefficients (ε) vary from ~110,000 to ~240,000 M⁻¹ cm⁻¹, in line with the high-absorption cross-sections characteristic for polymethine fluorophores.³⁴ The fluorescence quantum yields ($\Phi_{\rm F}$; relative

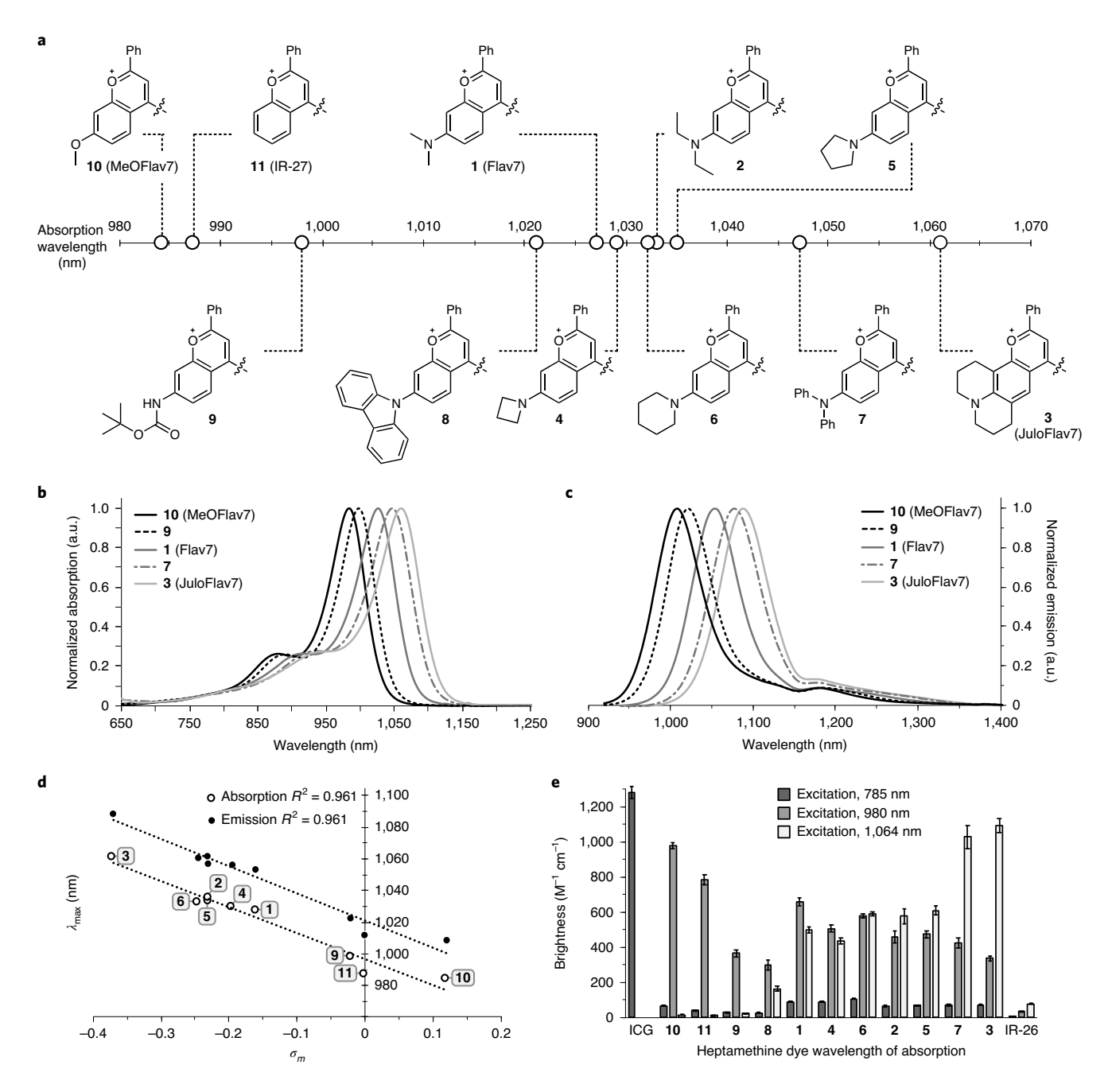


Fig. 2 | **Panel of flavylium heptamethine dyes and their photophysical properties. a**, Heterocycle structures and absorption wavelength maxima visualized graphically on the electromagnetic spectrum. **b,c**, Absorption (**b**) and emission (**c**) profiles (excitation wavelength, 885 nm) of selected polymethine dyes. **d**, Hammett plot relating σ_m substituent constants (ref. ⁵⁰) to absorption and emission wavelengths of dyes 1-6 and 9-11. **e**, Brightness (defined as $\varepsilon_\lambda \times \Phi_F$) of the heptamethine derivatives at relevant excitation wavelengths ($\lambda = 785$ nm (dark grey), $\lambda = 980$ nm (light grey) and $\lambda = 1,064$ nm (white)). Error bars represent the propagated error from standard deviations in ε and Φ_F measurements.

measurements to dye IR-26=0.05% (refs. 51,52); see Supplementary Note 3) remain rather constant, in the \sim 0.4–0.6% range. The combined high and relatively consistent ε and $\Phi_{\rm F}$ values result in a series of bright dyes spanning from 984–1,061 nm (Fig. 2b; Table 1), primed for real-time excitation multiplexing in the SWIR.

Excitation multiplexing with flavylium SWIR dyes. For excitation multiplexing, we are most interested in properties of the series of polymethine fluorophores when excited at 980 and 1,064nm, as these wavelengths correspond to readily available, low-cost and high-power (≥25 W) continuous-wave lasers and allow for

multiplexing with established dyes like ICG and IRDye 800CW at 785 or 808 nm. Thus, we calculated brightness(ϵ_{λ}) values for each dye using the absorption coefficient at the relevant wavelengths. The variation in brightness when excited at the wavelength of interest versus all other wavelengths used determines the amount of cross-talk between channels. Cross-talk reduces the contrast between channels, limiting the dynamic range. From Fig. 2e and Supplementary Fig. 1, we observe that Flav7 (1) has similar brightness when excited with 980 or 1,064 nm light, and thus is poorly suited for excitation multiplexing with these lasers. Examining Fig. 2e, candidates emerge for excitation-multiplexed imaging, with 3

ARTICLES <u>nature chemistry</u>

Table 1 | Photophysics of heptamethine fluorophores in dichloromethane

Dye	$\lambda_{\sf max,abs}$ (nm)	$arepsilon_{max}$ (M $^{-1}$ cm $^{-1}$) a	$\lambda_{ ext{max,em}}$ (nm)	$\Phi_{\scriptscriptstyle \sf F}$ (%) $^{\scriptscriptstyle \sf a}$	Brightness($\varepsilon_{\rm max}$) (M $^{-1}$ cm $^{-1}$) $^{\rm a}$
1 (Flav7)	1,027	241,000	1,053	0.61	1,470
2	1,033	190,000	1,057	0.62	1,180
3 (JuloFlav7)	1,061	238,000	1,088	0.46	1,090
4	1,029	207,000	1,056	0.51	1,060
5	1,034	247,000	1,061	0.48	1,190
6	1,032	110,000	1,060	0.54	590
7	1,047	210,000	1,078	0.58	1,220
8	1,021	140,000	1,048	0.45	630
9	998	108,000	1,022	0.42	450
10 (MeOFlav7)	984	190,000	1,008	0.52	990
11 (IR-27)	987	231,000	1,011	0.35	810
ICG	787 ^b	194,000 ^b	818 ^b	0.66 ^{b,c}	1,200°
IR-26	1,080	171,000	1,114	0.05 ^d	86

*See Supplementary Table 5 for errors in ε_{max} , Φ_p , and brightness(ε_{max}). Data taken from the literature (ethanol (EtOH)). Value includes the percent emission between 1,000 and 1,300 nm (5%)³⁷. Value from the literature (1,2-dichloroethane); treated as a constant for relative Φ_p measurements.

(named JuloFlav7) being superior for imaging at 1,064 nm (brigh tness(ϵ_{1064}) = 1,090 ± 40 M⁻¹ cm⁻¹) and 10 (named MeOFlav7) having the advantage at 980 nm (brightness(ϵ_{980}) = 980 ± 20 M⁻¹ cm⁻¹). We further analysed the photophysics of JuloFlav7 (3) for multiplexing using the percent difference of brightness at λ = 1,064 versus λ = 980 nm as a numerical metric to predict multiplexing performance and found that JuloFlav7 (3) is predicted to have the lowest levels of cross-talk compared to existing polymethine dyes (Supplementary Fig. 2)^{19,41}. This 'excitation-matching' concept can be further visualized by observing the absorption profiles and excitation wavelengths on the same plot (Fig. 3a). Employing ICG, which is well matched to the common 785 nm laser, adds a third colour.

To perform excitation multiplexing with single-channel SWIR detection using the new, bright SWIR-emissive dyes, a custom SWIR imaging configuration with three lasers and a fast InGaAs camera was constructed (Supplementary Fig. 3). With 785, 980 and 1,064 nm lasers, tailored excitation could preferentially excite three fluorophores. Emission is detected in a colour-blind fashion using identical filters and settings for all channels. This approach provides high-resolution images without optical aberrations arising from detection at different wavelengths (see Extended Data Figs. 2 and 3 and Supplementary Note 4 for multiplexing resolution effects). In addition, this method enables fast acquisition of all channels in each imaging frame by using rapidly modulated excitation sources and identical acquisition settings in a single detector. To accomplish real-time imaging, triggers on the millisecond timescale are sent independently to each continuous-wave laser, and the detector is programmed to collect a single frame for each sequential excitation pulse (Supplementary Note 5). While the effective frame rate of collection is slowed by a factor equal to the number of channels, video-rate acquisition was still achievable due to the well-matched, bright fluorophores.

In preparation for in vivo delivery of SWIR dyes, JuloFlav7 (3) and MeOFlav7 (10) were encapsulated in polyethylene glycol-coated micelles to impart water solubility (Supplementary Figs. 4 and 5). The micelle-encapsulated dyes demonstrate low toxicities to mammalian cells (Supplementary Fig. 6). The aqueous-soluble formulations of 3 and 10 display aggregation, which decreases the concentration of emissive species present in the aqueous environment, but does not substantially alter their excitation or emission profiles (Fig. 3b-d and Supplementary Fig. 7). We verified that

excitation multiplexing proceeded in both organic and aqueous environments by imaging tubes containing ICG (Fig. 3e, left), MeOFlav7 (10; centre) and JuloFlav7 (3; right) in organic solvent (top), and micelle encapsulations in water (middle). In each case, three successive frames collected with 785, 980 and 1,064 nm lasers show high intensities in the left, centre and right samples, respectively. Merging the three frames together yields a three-colour image representing one effective multiplexed frame. Because molecules absorb minimal light at energies lower than their S_0 to S_1 transition, cross-talk occurs primarily in one direction. Linear unmixing can correct for minor signal overlaps between channels as seen in Fig. 3e (bottom) and further discussed in the figure experimental procedures in the Supplementary Information.

In vivo demonstration of multicolour SWIR imaging. Using single-channel imaging, we validated that micelles containing JuloFlav7 (3) could be imaged with 8–9 ms exposure time after intravenous (i.v.) injection through a tail vein catheter in anaesthetized mice, under 1,064 nm excitation and 1,150–1,700 nm detection (Supplementary Video 1 and Extended Data Fig. 4). The high signal-to-noise ratio obtained at 100 fps was encouraging and suggested that video-rate speeds would be attainable upon addition of multiple channels. Further, the excitation-matching strategy was validated by an approximately tenfold improvement in speed compared to previously reported polymethine chromophores for imaging with 1,064 nm excitation (Supplementary Fig. 2).

We performed three-colour imaging in vivo by first performing an intraperitoneal (i.p.) injection of MeOFlav7 (10), followed by i.v. injections of JuloFlav7 (3) and finally ICG (Fig. 3f and Supplementary Videos 2 and 3). Representative time points of the three-colour video are displayed in Fig. 3g and Supplementary Fig. 8. The (bio)distribution of each dye over any position can be determined from the relative contributions of the three channels, as visualized in the single-channel images. After establishing both the technology and the molecular tools for multiplexed real-time observation of function in mice, the next goal was to enhance applications of SWIR imaging.

Applications of multicolour real-time SWIR imaging. Physiological properties such as heart rate, respiratory rate, thermoregulation, metabolism and central nervous system function are highly impacted by anaesthesia⁵³. Methods to observe animals in

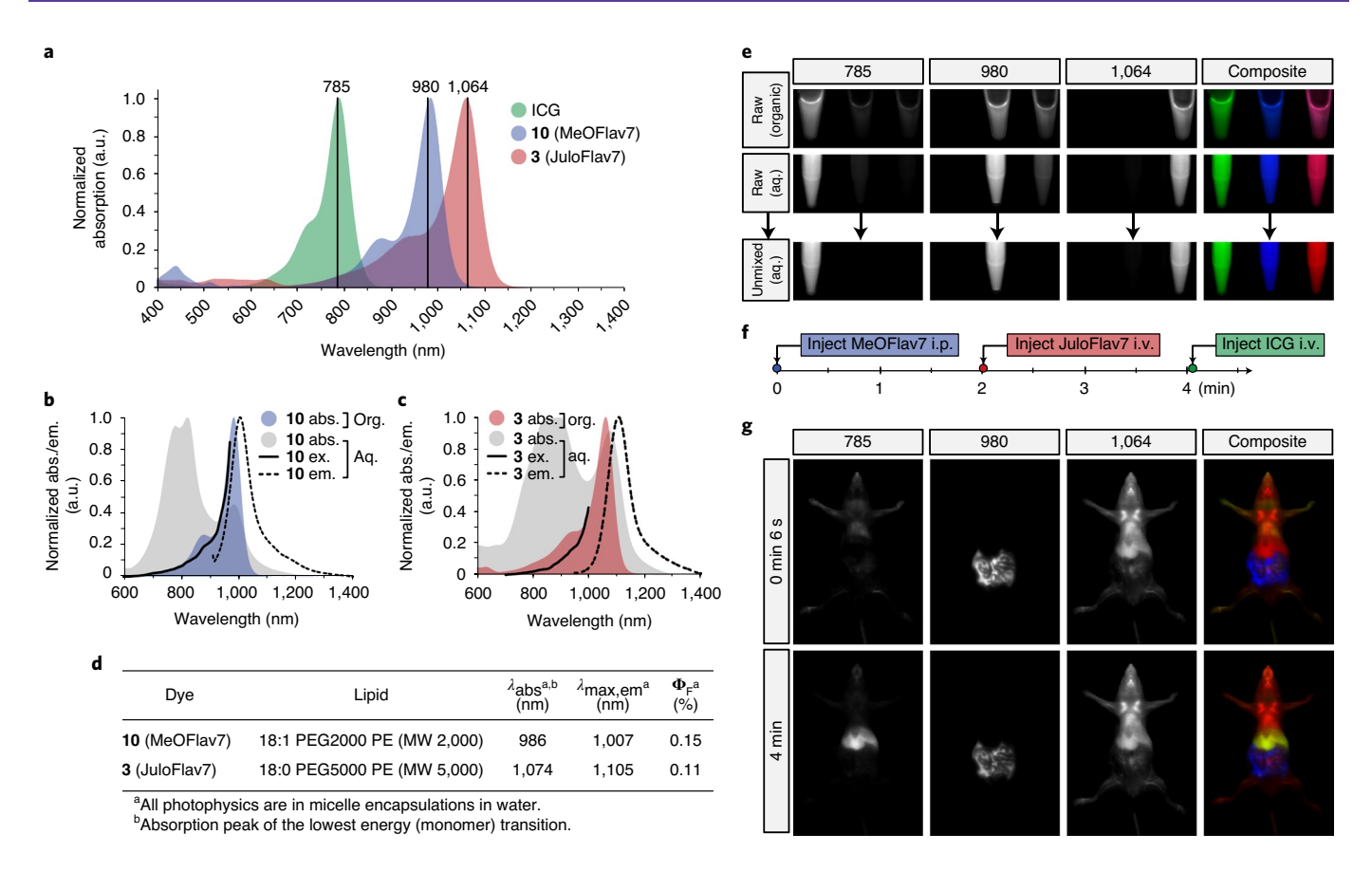


Fig. 3 | Excitation-multiplexed SWIR imaging. a, Absorption profiles of dyes used in imaging experiments plotted against excitation wavelengths employed. **b,c**, Absorption spectra (grey); emission spectra (excitation at 880 nm (b) and 900 nm (c), black dotted line); and excitation spectra (emission monitored at 1,008 nm (b) and 1,088 nm (c), black solid line) of micelle-encapsulated 10 (b) and 3 (c) overlaid with absorption traces of dyes in DCM (coloured). **d**, Photophysics of the micelle-encapsulated dyes in water. **e**, Raw and unmixed images of successive frames and merged three-colour images of vials containing ICG (left), 10 (centre) and 3 (right) in ethanol or DCM (top) and in micelles in water (middle and bottom). Arrows indicate linear unmixing procedure. **f**, Experimental timeline of administration of the three probes used in **g. g**, Multiplexed in vivo images using 785, 980 and 1,064 nm excitation wavelengths (average power density = 78 mW cm⁻²) and 1,150-1,700 nm collection (10 ms exposure time; 27.8 fps). Displayed images are averaged over five frames. Abs, absorption; em, emission; ex, excitation; org, organic; aq, aqueous; PEG, polyethylene glycol; PE, phosphoethanolamine; MW, molecular weight; λ_{abs}, wavelength of absorption maximum for the lowest energy (monomer) species; λ_{maxem}, wavelength of maximum emission.

their natural state are necessary to study physiology, but are currently limited to telemetric sensors and electrocardiography, involving surgical implantation⁵⁴ or external contact⁵⁵, respectively. Recently, high-speed SWIR imaging has enabled contact-free monitoring of physiology in awake mice¹⁸. Due to frame rates that are faster than macroscopic movements in animals, the heart rate and respiratory rate in awake animals can be quantified. In this study, we expanded this technique by observing awake, unperturbed mice in three colours. In Fig. 4a, Supplementary Fig. 9 and Supplementary Video 4, awake mouse imaging was performed 80 min after i.p. administration of MeOFlav7 (10) and consecutive i.v. administration of JuloFlav7 (3) and ICG. From the top view of the moving mouse, ICG could be visualized exclusively in the liver and MeOFlav7 (10) in the abdomen, while JuloFlav7 (3) remained systemically distributed throughout the mouse. In addition to the ability to assess natural physiology, such as the awake breathing rate (Fig. 4b, quantified here at 247 breaths per minute), contact free, these tools foreshadow more complex experiments in which the location of multiple probes could be monitored longitudinally, non-invasively and without

In addition, biodistribution of two species can be monitored in the same organs. For example, the accumulation and clearance from the liver of each probe can be observed and decoupled. We injected JuloFlav7 (3) and ICG consecutively through the tail vein and imaged the whole mouse at several time points over a one-hour period (Fig. 4c). In the duration of the experiment, the liver signal from the 1,064 channel remained constant, in contrast to the 785 channel, which shows depletion over time. (Fig. 4d and Supplementary Fig. 10). The fast acquisition speeds obtained via excitation multiplexing enable real-time (50 fps in two colours) feedback during necropsies and surgeries (Fig. 4e and Supplementary Video 5). The methods reported herein are applicable not only to non-invasive imaging but also in aiding surgeons in identifying essential and/or diseased structures during intraoperative procedures ^{56,57}.

A widely investigated use of fluorescence-guided surgery is for the lymphatic system, both to identify sentinel lymph nodes implicated in cancer⁵⁸ and to assess the structure/function of lymphatic networks in lymphovascular disorders⁵⁹. A complementary clinical need is to safely and quickly assess vascular function⁶⁰. With administration of ICG and JuloFlav7 (3) in the lymphatic and circulatory systems, respectively, both essential functions can be observed simultaneously. ICG was injected intradermally into the footpads and the tail. After 40 min, ICG had accumulated in the lymph system, and the pulsating motion of the collecting lymphatic vessels could be observed (Supplementary Video 6). Subsequently, JuloFlav7 (3) was injected intravenously, immediately filling the

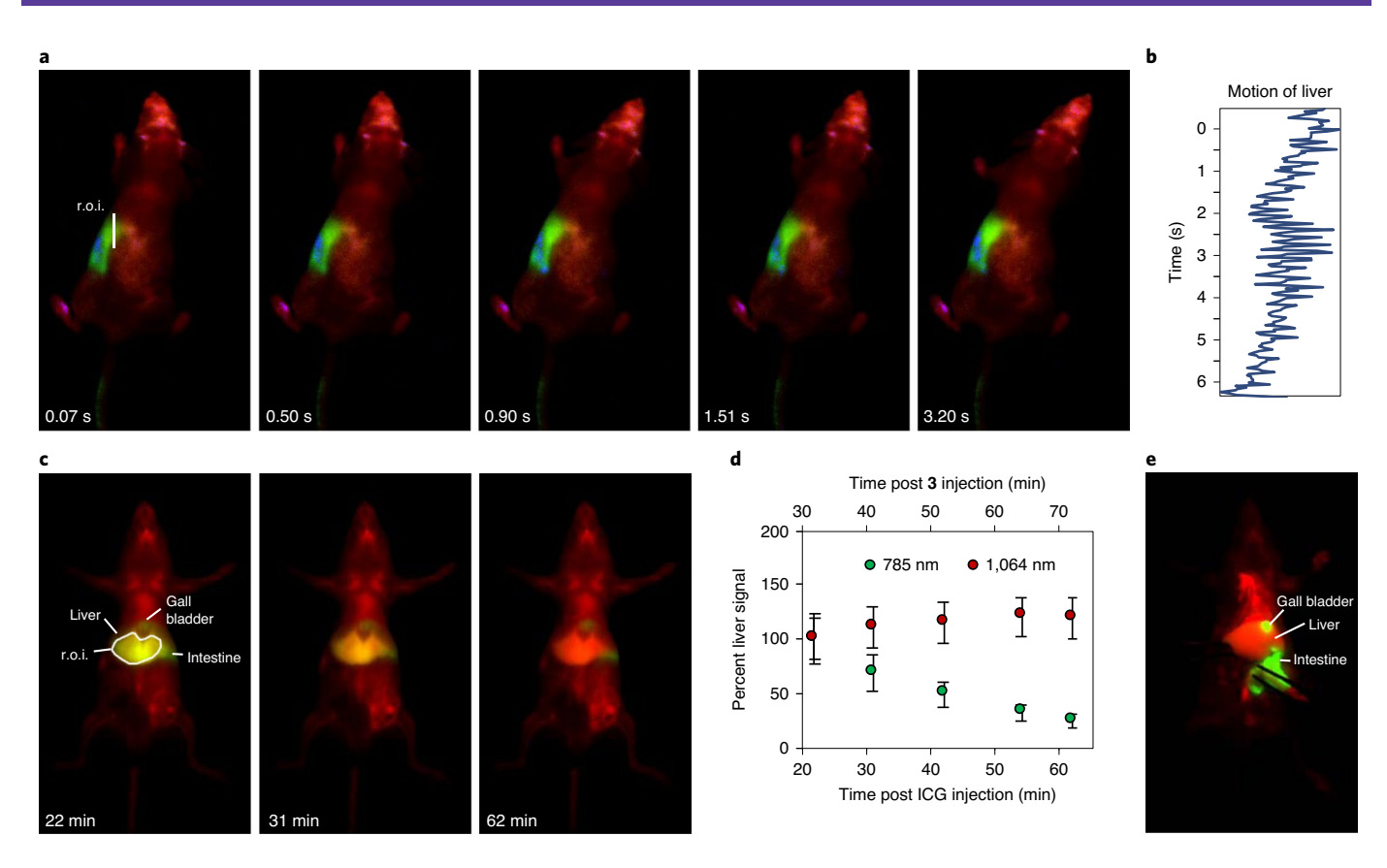


Fig. 4 | Applications enhanced by SWIR multiplexed imaging. a, Multiplexed imaging of an awake mouse showing one continuous movement of the head with 785, 980 and 1,064 nm excitation wavelengths (average power density = 78 mW cm⁻²) and 1,150–1,700 nm collection (10 ms exposure time; 27.8 fps). Displayed images are a single frame. **b**, Awake breathing rate (247 breaths per minute), analysed by quantifying the liver motion (by the centre of mass) over the region of interest (r.o.i.) in **a. c**, Imaging of ICG clearance with systemic labelling by JuloFlav7 (3) micelles. Multiplexed in vivo images using 785 and 1,064 nm excitation (100 mW cm⁻²) and 1,150–1,700 nm collection (5 ms exposure time; 50 fps). Displayed images are averaged over five frames. **d**, Percent signal in the liver of ICG and micelles of JuloFlav7 (3) over one hour. Data are displayed as the mean intensity over the r.o.i. (in **c**) \pm standard deviation, n = 805 pixels within the r.o.i. **e**, Two-colour necropsy procedure, captured in real time in Supplementary Video 5. Acquisition settings are as in **c**.

vasculature (Fig. 5a-c, Supplementary Fig. 11 and Supplementary Video 6). Image collection at 21 fps in two channels gave high spatially and temporally resolved images with separate visualization of lymph vessels from veins and arteries (Fig. 5d-e and Supplementary Fig. 12). Notably, the function of each vessel, modelled by the signal across a linear cross-section, can be observed in real time (Fig. 5f). The ability to differentiate lymph and circulatory structures and simultaneously monitor their function has implications in non-invasive diagnostics as well as in expanding technologies for fluorescence-guided surgery.

Discussion

Despite the large set of optical tools developed for the VIS and NIR regions of the electromagnetic spectrum, which enable fast, multiplexed detection in small model organisms, non-invasive, multicolour imaging in mammals with high resolution is still a considerable challenge. By developing predictably tunable SWIR polymethine fluorophores, along with a triggered multi-excitation SWIR optical configuration, we demonstrated multicolour whole-animal imaging at video-rate speeds and sub-millimetre resolution. The approach of excitation multiplexing with single-channel SWIR detection presented here minimizes challenges due to the low quantum yields of SWIR fluorophores by using efficient excitation and detection, and also expands the wavelengths of the electromagnetic spectrum compatible with multicolour deep-tissue imaging.

Several key advances were necessary to successfully translate excitation-multiplexed imaging methods to whole animals. The ability to fine-tune the spectral properties of the fluorophores to excitation-match relevant lasers was accomplished by systematic functional group manipulation on a bright SWIR dye scaffold. These studies revealed predictive metrics for SWIR fluorophore absorption/emission using physical organic chemistry and produced MeOFlav7 (10), well matched to 980 nm, and JuloFlav7 (3), well matched to 1,064 nm. These dyes, along with FDA-approved ICG, enable single-channel imaging at 100 fps and two- or three-colour imaging at video-rate speeds (≥27 fps). Ultimately, we envision that excitation-matching will be an essential design principle for the future optimization and utility of fluorophores and other light-activated probes.

The technologies open a new realm in monitoring orthogonal function in mammals, even in awake animals without restraint or implantation. Furthermore, the rapid acquisition speeds combined with the high spatial resolution at which multiplexed imaging can be performed will enable real-time information regarding the localization of tagged biomolecules, labelled structures (for example, a tumour) and anatomical reference structures such as tissues (for example, liver or bones) and blood and lymphatic vessels. These tools, as well as further exploration of polymethine-based probes and the development of clinical imaging systems, will enable superior surgical, diagnostic and biomedical studies.

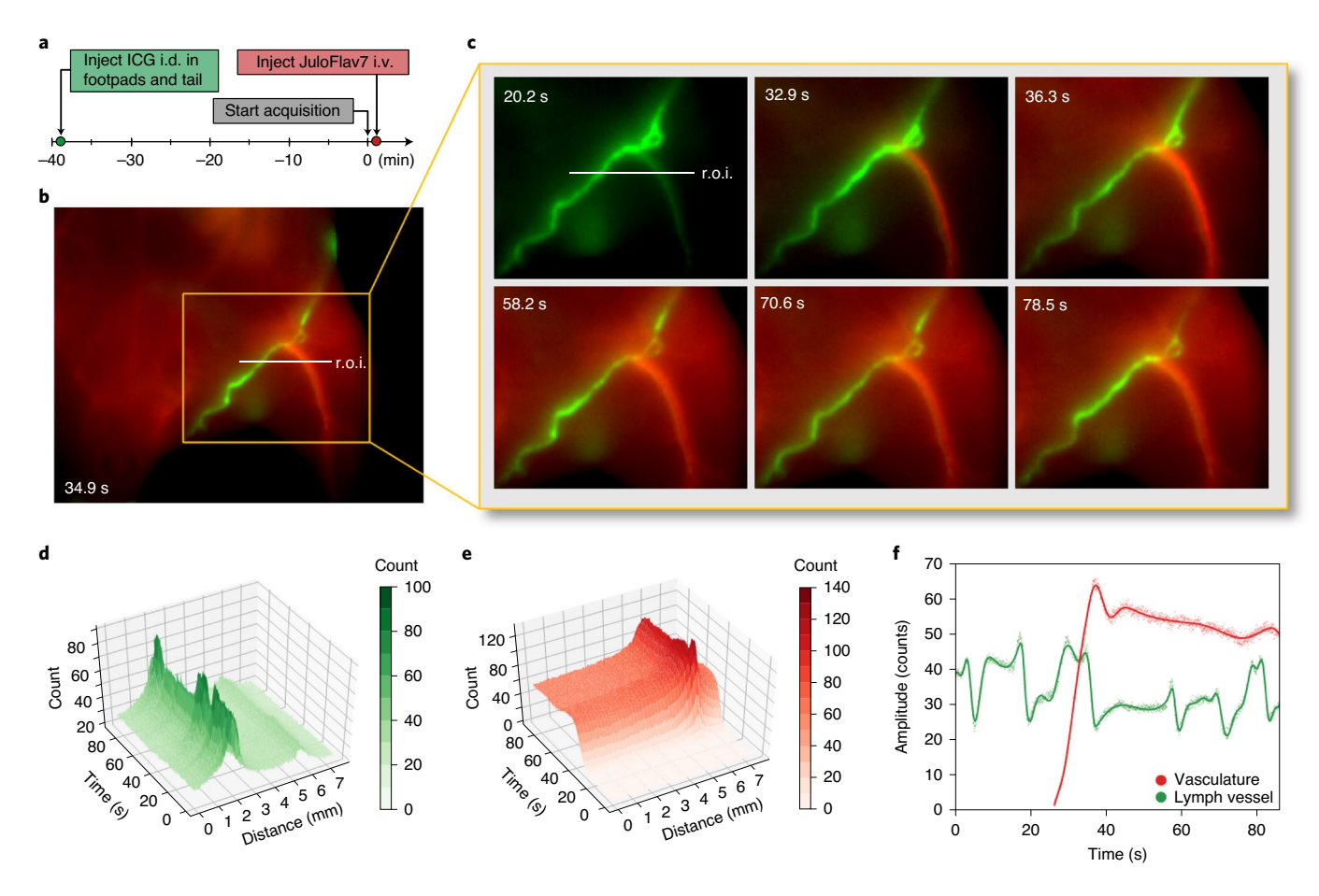


Fig. 5 | Orthogonal lymphatic and circulatory imaging with high spatiotemporal resolution after intradermal (i.d.) injection of ICG and i.v. injection of JuloFlav7 (3) micelles. a, Experimental timeline. **b**, Representative image acquired 30 s after injection of JuloFlav7 (3) micelles. **c**, Time points over the relevant time period analysed in **d-f. d,e**, Three-dimensional plots of the 785 nm channel (**d**) and 1,064 nm channel (**e**) demonstrating simultaneous intensity information in two colours over the r.o.i. indicated in **b** and **c**, and highlighting the spatial and temporal resolution captured. Contour plots are shown in Supplementary Fig. 9. **f**, The signal in each vessel over time can be quantified by plotting the amplitude of the vessel, fit as a Gaussian curve at each frame (points). The data is interpolated using a smoothing spline fit (solid lines). Acquisition, 785 and 1,064 nm excitation wavelengths (96 mW cm⁻²) and 1,100–1,700 nm collection (20 ms exposure time; 21.7 fps). Displayed images are averaged over five frames.

Online content

Any methods, additional references, Nature Research reporting summaries, source data, extended data, supplementary information, acknowledgements, peer review information; details of author contributions and competing interests; and statements of data and code availability are available at https://doi.org/10.1038/s41557-020-00554-5.

Received: 24 September 2019; Accepted: 17 August 2020; Published online: 19 October 2020

References

- Dean, K. M. & Palmer, A. E. Advances in fluorescence labeling strategies for dynamic cellular imaging. Nat. Chem. Biol. 10, 512–523 (2014).
- 2. Wei, L. et al. Super-multiplex vibrational imaging. Nature 544, 465-470 (2017).
- Frangioni, J. V. In vivo near-infrared fluorescence imaging. Curr. Opin. Chem. Biol. 7, 626–634 (2003).
- Kong, L. et al. Continuous volumetric imaging via an optical phase-locked ultrasound lens. Nat. Methods 12, 759–762 (2015).
- Grimm, J. B. et al. A general method to fine-tune fluorophores for live-cell and in vivo imaging. Nat. Methods 14, 987–994 (2017).
- Fenrich, K. K. et al. Long-term in vivo imaging of normal and pathological mouse spinal cord with subcellular resolution using implanted glass windows. *I. Physiol.* 590, 3665–3675 (2012).
- Rakhymzhan, A. et al. Synergistic strategy for multicolor two-photon microscopy: application to the analysis of germinal center reactions in vivo. Sci. Rep. 7, 7101 (2017).

- Kim, P., Puoris'haag, M., Côté, D., Lin, C. P. & Yun, S. H. In vivo confocal and multiphoton microendoscopy. J. Biomed. Opt. 13, 010501 (2008).
- Kosaka, N., Ogawa, M., Sato, N., Choyke, P. L. & Kobayashi, H. In vivo real-time, multicolor, quantum dot lymphatic imaging. *J. Invest. Dermatol.* 129, 2818–2822 (2009).
- Erogbogbo, F. et al. In vivo targeted cancer imaging, sentinel lymph node mapping and multi-channel imaging with biocompatible silicon nanocrystals. ACS Nano 5, 413–423 (2011).
- Shcherbakova, D. M. & Verkhusha, V. V. Near-infrared fluorescent proteins for multicolor in vivo imaging. Nat. Methods 10, 751–754 (2013).
- Zavaleta, C. L. et al. Multiplexed imaging of surface enhanced Raman scattering nanotags in living mice using noninvasive Raman spectroscopy. *Proc. Natl Acad. Sci. USA* 106, 13511–13516 (2009).
- Zhang, H. et al. Penetration depth of photons in biological tissues from hyperspectral imaging in shortwave infrared in transmission and reflection geometries. J. Biomed. Opt. 21, 126006 (2016).
- Carr, J. A. et al. Absorption by water increases fluorescence image contrast of biological tissue in the shortwave infrared. *Proc. Natl Acad. Sci. USA* 115, 9080–9085 (2018).
- Naczynski, D. J. et al. Rare-earth-doped biological composites as in vivo shortwave infrared reporters. Nat. Commun. 4, 2199 (2013).
- Welsher, K. et al. A route to brightly fluorescent carbon nanotubes for near-infrared imaging in mice. Nat. Nanotechnol. 4, 773–780 (2009).
- Hong, G. et al. In vivo fluorescence imaging with Ag₂S quantum dots in the second near-infrared region. *Angew. Chem. Int. Ed.* 51, 9818–9821 (2012).
- Bruns, O. T. et al. Next-generation in vivo optical imaging with short-wave infrared quantum dots. Nat. Biomed. Eng. 1, 0056 (2017).

- Tao, Z. et al. Biological imaging using nanoparticles of small organic molecules with fluorescence emission at wavelengths longer than 1000 nm. *Angew. Chem. Int. Ed.* 52, 13002–13006 (2013).
- Yang, Q. et al. Rational design of molecular fluorophores for biological imaging in the NIR-II window. Adv. Mater. 29, 1605497 (2017).
- Zhu, S. et al. 3D NIR-II molecular imaging distinguishes targeted organs with high-performance NIR-II bioconjugates. Adv. Mater. 30, 1705799 (2018).
- Wan, H. et al. A bright organic NIR-II nanofluorophore for three-dimensional imaging into biological tissues. *Nat. Commun.* 9, 1171 (2018).
- 23. Wang, F. et al. Light-sheet microscopy in the near-infrared II window. *Nat. Methods* **16**, 545–552 (2019).
- 24. Zhu, S. et al. Molecular imaging of biological systems with a clickable dye in the broad 800- to 1,700-nm near-infrared window. *Proc. Natl Acad. Sci. USA* 114. 962–967 (2017).
- Ma, B. L., Zhai, X., Du, G. & Zhou, J. Orthogonal shortwave infrared emission based on rare earth nanoparticles for interference-free logical codes and bio-imaging. *Chem. Sci.* 10, 3281–3288 (2019).
- Hong, G. et al. Through-skull fluorescence imaging of the brain in a new near-infrared window. *Nat. Photonics* 8, 723–730 (2014).
- near-infrared window. *Nat. Photonics* **8**, 723–730 (2014).

 27. Diao, S. et al. Fluorescence imaging in vivo at wavelengths beyond 1500 nm. *Angew. Chem. Int. Ed.* **54**, 14758–14762 (2015).
- 28. Kapanidis, A. N. et al. Alternating-laser excitation of single molecules. *Acc. Chem. Res.* **38**, 523–533 (2005).
- 29. Müller, B. K., Zaychikov, E., Bräuchle, C. & Lamb, D. C. Pulsed interleaved excitation. *Biophys. J.* 89, 3508–3522 (2005).
- Lewis, E. K. et al. Color-blind fluorescence detection for four-color DNA sequencing. Proc. Natl Acad. Sci. USA 102, 5346–5351 (2005).
- Garbacik, E. T., Sanz-Paz, M., Borgman, K. J. E., Campelo, F. & Garcia-Parajo, M. F. Frequency-encoded multicolor fluorescence imaging with singlephoton-counting color-blind detection. *Biophys. J.* 115, 725–736 (2018).
- Gómez-García, P. A., Garbacik, E. T., Otterstrom, J. J., Garcia-Parajo, M. F. & Lakadamyali, M. Excitation-multiplexed multicolor superresolution imaging with fm-STORM and fm-DNA-PAINT. *Proc. Natl Acad. Sci. USA* 115, 12991–12996 (2018).
- Thimsen, E., Sadtler, B. & Berezin, M. Y. Shortwave-infrared (SWIR) emitters for biological imaging: a review of challenges and opportunities. *Nanophotonics* 6, 1043–1054 (2017).
- Bricks, J. L., Kachkovskii, A. D., Slominskii, Y. L., Gerasov, A. O. & Popov, S. V. Molecular design of near infrared polymethine dyes: a review. *Dyes Pigm.* 121, 238–255 (2015).
- Marshall, M. V. et al. Near-infrared fluorescence imaging in humans with indocyanine green: a review and update. Open Surg. Oncol. J. 2, 12–25 (2010).
- Rurack, K. & Spieles, M. Fluorescence quantum yields of a series of red and nearinfrared dyes emitting at 600–1000 nm. Anal. Chem. 83, 1232–1242 (2011).
- Carr, J. A. et al. Shortwave infrared fluorescence imaging with the clinically approved near-infrared dye indocyanine green. *Proc. Natl Acad. Sci. USA* 115, 4465–4470 (2018).
- Starosolski, Z. et al. Indocyanine green fluorescence in second near-infrared (NIR-II) window. PLOS One 12, e0187563 (2017).
- Cosco, E. D. et al. Flavylium polymethine fluorophores for near- and shortwave infrared imaging. *Angew. Chem. Int. Ed.* 56, 13126–13129 (2017).
- Henary, M., Mojzych, M., Say, M. & Strekowski, L. Functionalization of benzo[c,d]indole system for the synthesis of visible and near-infrared dyes. J. Heterocycl. Chem. 46, 84–87 (2009).
- Li, B., Lu, L., Zhao, M., Lei, Z. & Zhang, F. An efficient 1064 nm NIR-II excitation fluorescent molecular dye for deep-tissue high-resolution dynamic bioimaging. *Angew. Chem. Int. Ed.* 57, 7483–7487 (2018).

- Ding, B. et al. Polymethine thiopyrylium fluorophores with absorption beyond 1000 nm for biological imaging in the second near-infrared subwindow. J. Med. Chem. 62, 2049–2059 (2019).
- Wang, S. et al. Anti-quenching NIR-II molecular fluorophores for in vivo high-contrast imaging and pH sensing. *Nat. Commun.* 10, 1058 (2019).
- Lei, Z. et al. Stable, wavelength-tunable fluorescent dyes in the NIR-II region for in vivo high-contrast bioimaging and multiplexed biosensing. *Angew. Chem. Int. Ed.* 58, 8166–8171 (2019).
- Chen, J.-R., Wong, J.-B., Kuo, P.-Y. & Yang, D.-Y. Synthesis and characterization of coumarin-based spiropyran photochromic colorants. Org. Lett. 10, 4823–4826 (2008).
- Roehri-Stoeckel, C., Gonzalez, E. & Fougerousse, A. Synthetic dyes: simple and original ways to 4-substituted flavylium salts and their corresponding vitisin derivatives. Can. J. Chem. 79, 1173–1178 (2001).
- Seijas, J. A., Vázquez-Tato, M. P. & Carballido-Reboredo, R. Solvent-free synthesis of functionalized flavones under microwave irradiation. *J. Org. Chem.* 70, 2855–2858 (2005).
- Kónya, K., Pajtás, D., Kiss-Szikszai, A. & Patonay, T. Buchwald-Hartwig reactions of monohaloflavones. Eur. J. Org. Chem. 2015, 828–839 (2015).
- Kopainsky, B., Qiu, P., Kaiser, W., Sens, B. & Drexhage, K. H. Lifetime, photostability, and chemical structure of IR heptamethine cyanine dyes absorbing beyond 1 μm. *Appl. Phys. B* 29, 15–18 (1982).
- Hansch, C., Leo, A. & Taft, R. W. A survey of Hammett substituent constants and resonance and field parameters. *Chem. Rev.* 91, 165–195 (1991).
- Semonin, O. E. et al. Absolute photoluminescence quantum yields of IR-26 Dye, PbS, and PbSe quantum dots. J. Phys. Chem. Lett. 1, 2445–2450 (2010).
- Hatami, S. et al. Absolute photoluminescence quantum yields of IR26 and IR-emissive Cd_{1-x}Hg_xTe and PbS quantum dots – method- and material-inherent challenges. *Nanoscale* 7, 133–143 (2015).
- Lukasik, V. M. & Gillies, R. J. Animal anaesthesia for in vivo magnetic resonance. NMR Biomed. 16, 459–467 (2003).
- Schwenke, D. O., Pearson, J. T., Mori, H. & Shirai, M. Long-term monitoring of pulmonary arterial pressure in conscious, unrestrained mice. *J. Pharmacol. Toxicol. Methods* 53, 277–283 (2006).
- Sato, M. et al. Simultaneous monitoring of mouse respiratory and cardiac rates through a single precordial electrode. *J. Pharmacol. Sci.* 137, 177–186 (2018)
- Ceppi, L. et al. Real-time single-walled carbon nanotube-based fluorescence imaging improves survival after debulking surgery in an ovarian cancer model. ACS Nano 13, 5356–5365 (2019).
- Zhu, S., Tian, R., Antaris, A. L., Chen, X. & Dai, H. Near-infrared-II molecular dyes for cancer imaging and surgery. Adv. Mater. 31, e1900321 (2019).
- Cousins, A., Thompson, S. K., Wedding, A. B. & Thierry, B. Clinical relevance of novel imaging technologies for sentinel lymph node identification and staging. *Biotechnol. Adv.* 32, 269–279 (2014).
- Rasmussen, J. C., Fife, C. E. & Sevick-Muraca, E. M. Near-infrared fluorescence lymphatic imaging in lymphangiomatosis. *Lymphat. Res. Biol.* 13, 195–201 (2015).
- Tozzi, M., Boni, L., Soldini, G., Franchin, M. & Piffaretti, G. Vascular fluorescence imaging control for complex renal artery aneurysm repair using laparoscopic nephrectomy and autotransplantation. *Case Rep. Transplant*. 2014, 563408 (2014).

Publisher's note Springer Nature remains neutral with regard to jurisdictional claims in published maps and institutional affiliations.

© The Author(s), under exclusive licence to Springer Nature Limited 2020

Methods

Materials. Chemical reagents were purchased from Accela, Acros Organics, Alfa Aesar, Carl Roth, Fisher Scientific, Sigma-Aldrich or TCI and used without purification unless noted otherwise. Lipids were purchased from Laysan Bio and Avanti Polar Lipids. Anhydrous and deoxygenated solvents (toluene, THF) were dispensed from a Grubb's-type Phoenix Solvent Drying System constructed by J. C. Meyer. Anhydrous solvents were prepared by drying over 4 Å molecular sieves for at least three days (1,4-dioxane, ethanol, *n*-butanol, *n*-pentanol) or dried with CaCl₂, followed by MgSO₄ and distilled (EtOAc). Oxygen was removed by three consecutive freeze–pump–thaw cycles in air-free glassware directly before use.

Instrumentation. Thin layer chromatography was performed using Silica Gel 60 F₂₅₄ (EMD Millipore) plates. Flash chromatography was executed with technical grade silica gel with 60 Å pores and 40-63 μm mesh particle size (Sorbtech Technologies). Solvent was removed under reduced pressure with a Büchi Rotavapor with a Welch self-cleaning dry vacuum pump and further dried with a Welch DuoSeal pump. Bath sonication was performed using a Branson 3800 ultrasonic cleaner or an Elma S15Elmasonic. Nuclear magnetic resonance (1H NMR, 13C NMR and 19F NMR) spectra were taken on a Bruker Avance 300, AV-400, AV-500 or AV-600 instrument and processed with MestReNova or TopSpin software. All ¹H NMR and ¹³C NMR peaks are reported in ppm in reference to their respective solvent signals. The 19F NMR spectra are reported in ppm in reference to α,α,α -trifluorotoluene at -63.90 ppm as an external standard⁶¹. High-resolution mass spectra (electrospray ionization) were obtained on a Thermo Scientific Q Exactive Plus Hybrid Quadrupole-Orbitrap M with Dionex UltiMate 3000 RSLCnano System. Infrared spectra were obtained on a PerkinElmer UATR Two FT-IR spectrometer and are reported in terms of frequency of absorption (cm⁻¹). Nanomaterial size was analysed with a Malvern Zetasizer Nano dynamic light scattering instrument in plastic 1 cm cuvettes. Absorption spectra were collected on a JASCO V-770 UV-visible/NIR spectrophotometer with a 2,000 nm min⁻¹ scan rate after blanking with the appropriate solvent. Photoluminescence spectra were obtained on a Horiba Instruments PTI QuantaMaster Series fluorometer. Quartz cuvettes $(10 \text{ mm} \times 10 \text{ mm}, 2 \text{ mm} \times 10 \text{ mm} \text{ or } 3 \text{ mm} \times 3 \text{ mm}; \text{Starna Cells or Thorlabs})$ were used for absorption and photoluminescence measurements. All spectra were obtained at ambient temperature. Normalized spectra are displayed for clarity. Absorption coefficient ($\varepsilon_{\rm max}$) values in DCM were calculated using serial dilutions with Hamilton syringes in volumetric glassware and are displayed as the mean \pm standard deviation (n=3 measurements). Relative quantum yields were determined in DCM relative to IR-26 in DCM. See Supplementary Note 3 for a detailed discussion of quantum yield measurements.

General synthetic procedures. Flavones 13a-c were synthesized by subjecting the corresponding 3-aminophenol (150-750 mg scale, 1.0 equiv.) to ethyl benzoylacetate (1.75-2.0 equiv.) and heating at 180 °C for 15-48 h. Compounds were purified by column chromatography with a hexanes/EtOAc solvent gradient (51–55% yield; see Supplementary Table 1). Flavone 15 was synthesized following a known procedure⁶² from 7-hydroxyflavone 16. Flavones 13d-h were synthesized by subjecting flavone 15 (50-180 mg scale, 1.0 equiv.) to the corresponding secondary amine (1.5-2.8 equiv.), RuPhos Pd G3 (0.1 equiv.), RuPhos (0.1 equiv.) and caesium carbonate (1.5 equiv.), in either toluene (at 100-110 °C; 0.1-0.3 M) or THF (at 50 °C; 0.1-0.3 M) for 5.5-22 h. Compounds were purified by column chromatography with a hexanes/EtOAc solvent gradient (63-83% yield; see Supplementary Table 2). Flavone 13i was synthesized by subjecting 7-aminoflavone (17) (180 mg scale, 1.0 equiv.) to di-tert-butyl dicarbonate (3.2 equiv.), triethylamine (2.5 equiv.) and dimethylamino pyridine (0.3 equiv.) in THF (0.2 M), and heating to reflux for 48 h. The compound was purified by column chromatography with a hexanes/EtOAc solvent gradient (66% yield).

Flavyliums 12a–i were synthesized by subjecting the corresponding flavone (13a–i) (20–770 mg scale, 1.0 equiv.) to methyl magnesium bromide (1.5–3.2 equiv.) in THF (0.05–0.1 M) at 0 °C, warming to room temperature and stirring for 12–24h. The reaction was quenched with aqueous fluoroboric acid, extracted with DCM and aqueous fluoroboric acid, dried and filtered. The compounds were purified by trituration with EtOAc or with diethyl ether and toluene (39–86% yield, 12i not isolated for yield; see Supplementary Table 3). Flavylium 12j was synthesized following a literature procedure 45 .

Heptamethine dyes **1–11** were synthesized by subjecting the corresponding flavylium (**12a–j**) (10–150 mg scale, 1.0 equiv.) to *N*-((3-(anilinomethylene)-2-chloro-1-cyclohexen-1-yl)methylene)aniline hydrochloride (**18**) (0.40–0.49 equiv.) with either sodium acetate or 2,6-di-*tert*-butyl-4-methylpyridine (1.5–5.6 equiv.) with either *n*-butanol/toluene, 1,4-dioxane, ethanol or *n*-pentanol (0.05–0.1 M) at 70–140 °C for 10–120 min. Compounds were purified by a mixture of column chromatography (with a gradient of either DCM/EtOH, DCM/acetone, DCM/MeCN or DCM/toluene/EtOH), trituration (in toluene and THF) and Soxhlet extraction (compound **10**, in toluene). Compunds were isolated in 5–51% yield (see Supplementary Table 4). See the synthetic procedures and characterization in the Supplementary Information for individual procedures used to obtain each flavone, flavylium and heptamethine dye and the full characterization of all new compounds.

Animal procedures. Animal experiments were conducted in conformity with the institutional guidelines. Non-invasive whole mouse imaging was performed on athymic nude female mice (6–16 weeks old, weight between 20–25 g), purchased from Envigo. Mice were anaesthetized with an i.p. injection of a ketamine/xylazine mixture. Tail vein injections were performed with a catheter assembled from a 30-gauge needle connected through plastic tubing to a syringe prefilled with isotonic saline solution. The bevel of the needle was then inserted into the tail vein and secured using tissue adhesive. The plastic tubing was then connected to a syringe (30-gauge needle) prefilled with the probe of interest. All probes were filtered through a 0.22 µm syringe filter prior to i.v. injection.

SWIR imaging apparatus. For whole mouse imaging, a custom-built set-up was used. Lumics laser units (LU1064DLD350-S70AN03 (35 W), 1,064 nm; LU0980D350-D30AN (35 W), 980 nm; and LU0785DLU250-S70AN03 (25 W), 785 nm) were used for excitation. Laser modules are specced to ±10 nm. Laser outputs were coupled in a 4×1 fan-out fibre-optic bundle (Thorlabs BF46LS01) of 600 µm core diameter for each optical path. The output from the fibre was fixed in an excitation cube (Thorlabs KCB1EC/M), reflected off of a mirror (Thorlabs BBE1-E03) and passed through a positive achromat (Thorlabs AC254-050-B), SP filter (if necessary) and ground glass diffuser (Thorlabs DG10-120-MD) or an engineered diffuser (Thorlabs ED1-S20-MD) to provide uniform illumination over the working area. In a typical experiment, the excitation flux at the object was adjusted to be close to $100 \,\mathrm{mW \, cm^{-2}}$ with an error of $\pm 3\%$ (the power density used is defined separately in each experiment). The working area was covered by a heating mat coated with blackout fabric (Thorlabs BK5). Emitted light was directed onto an Allied Vision Goldeye G-032 Cool TEC2 camera with a sensor temperature set point of -20°C.

Two lens systems were used, as follows:

Lens system A: emitted light was directed through a four-inch square first-surface silver mirror (Edmund Optics, 84448) with a custom filter set (defined for each experiment) and a C-mount camera lens (Navitar, SWIR-35).

Lens system B: the custom lens system consists of a 4f configuration with three lenses with focal length $(f) = 500.0\,\mathrm{mm}$ (Thorlabs LB1909-C) and two $f = 200.0\,\mathrm{mm}$ lenses (Thorlabs LB1199-C) with a custom filter set (defined for each experiment). For ergonomic reasons, a 2 inch protected silver-coated elliptical mirror (PFE20-P01) mounted to a kinematic mount (Thorlabs KCB2EC/M) was used.

The assembly was partially enclosed to avoid excess light while enabling manipulation of the field of view during operation. The image acquisition toolbox of the MATLAB programming environment was used in combination with a custom MATLAB script to preview and collect the required image data in 8-bit or 12-bit format. The prepared MATLAB script allows users to access basic functionalities of the image acquisition device by establishing the necessary communication layer and a stable streaming link between the host computer and the imaging device.

Multiplexed imaging acquisition. To facilitate real-time multiplexed imaging, a programmable trigger controller was implemented using an Arduino Nano Rev 3 (A000005) microcontroller unit. Predetermined triggering sequences written in C language were compiled using the Arduino Integrated Development Environment in the host computer and uploaded via USB interface to the microcontroller unit. The pre-programmed trigger controller was then used to deliver the sequential electrical voltage signals of 5 V to the laser driver units and InGaAs camera to perform multiplexed image acquisition. A semi-automatic imaging algorithm adopted in MATLAB (see above, SWIR imaging apparatus), in combination with manual control of laser parameters via the individual laser modules, and the programmed microcontroller unit facilitate excitation-synchronized imaging. Excitation-synchronized frames are collected by the camera and transferred to the personal computer via the GigE interface. Further information and illustrative figures can be found in Supplementary Note 5.

Image processing procedures. Images were processed using the Fiji distribution⁶³ of ImageJ⁶⁴. All images were background corrected with a ten-frame averaged background file to correct for non-linearities in the detector and/or excitation. Raw images underwent no further processing. Unmixed images were image subtracted according to the relative contribution of each channel, determined separately for each experiment, and detailed in the Supplementary Information, in the figure experimental procedures. All still images were averaged over five frames and converted to 8-bit PNG files for display, unless stated otherwise. Videos were frame averaged to reduce file size, if necessary, before compression with FFmpeg to a .mov file.

Additional methods information included in the Supplementary Information file includes experimental procedures specific to each figure, supplementary figures and supplementary videos, supplementary notes that contain a synthetic procedure discussion, Hammett plot calculations, SWIR imaging with triggered excitation multiplexing, the photoluminescence quantum yields and the synthetic procedures and characterization.

Reporting Summary. Further information on research design is available in the Nature Research Reporting Summary linked to this article.

Data availability

Image datasets, including all raw and processed imaging data generated in this work, are available at BioImage Archive (accession number: S-BIAD27). All other datasets that support the findings of this study are contained within the manuscript and its Supplementary Information.

Code availability

Custom computer programs used for the work are available at GitHub (https://gitlab.com/brunslab/ccda).

References

- Bexrud, J. A., Eisenberger, P., Leitch, D. C., Payne, P. R. & Schafer, L. L. Selective C-H activation α to primary amines. Bridging metallaaziridines for catalytic, intramolecular α-alkylation. *J. Am. Chem. Soc.* 131, 2116–2118 (2009).
- Kövér, J. & Antus, S. Facile deoxygenation of hydroxylated flavonoids by palladium-catalysed reduction of its triflate derivatives. Z. Naturforsch. 60b, 792–796 (2005).
- Schindelin, J. et al. Fiji: an open-source platform for biological-image analysis. Nat. Methods 9, 676–682 (2012).
- Rueden, C. T. et al. ImageJ2: ImageJ for the next generation of scientific image data. BMC Bioinf. 18, 529 (2017).

Acknowledgements

This work was supported by grants to E.D.C. (NSF GRFP DGE-1144087, Christopher S. Foote Fellowship), O.T.B. (Emmy-Noether-Programme of DFG BR 5355/2-1, Helmholtz Pioneer Campus Institute for Biomedical Engineering), E.M.S. (UCLA, Sloan Research Award FG-2018-10855, NIH 1R01EB027172-01) and Helmholtz Zentrum

München, and by shared instrumentation grants from the NSF (CHE-1048804) and NIH (1S10OD016387-01). We thank T. Schwarz-Romond, T. S. Bischof, D. Bengel (Helmholtz Zentrum München), K. N. Houk, J. R. Caram (UCLA) and L. D. Lavis (Janelia) for discussions and support and the Garcia-Garibay Group (UCLA) for instrumentation.

Author contributions

E.D.C., E.M.S. and O.T.B. designed the study. E.M.S. and O.T.B. jointly advised the study. E.D.C., A.L.S., M.P. and R.R.M. performed the synthesis. E.D.C. measured and analysed the photophysics. S.R. developed the software and built electronics and instrumentation. E.D.C., J.G.P.L. and M.W. built optical configurations. E.D.C., M.S., B.A.A. and S.G. performed imaging experiments. E.D.C., J.G.P.L. and B.A.A. analysed images. K.C.Y.W. performed cell culture experiments. E.D.C., E.M.S. and O.T.B. wrote and edited the paper. E.M.S., O.T.B. and V.N. provided funding. All authors have given approval to the final version of the manuscript. Correspondence and requests for materials should be addressed to E.M.S and O.T.B.

Competing interests

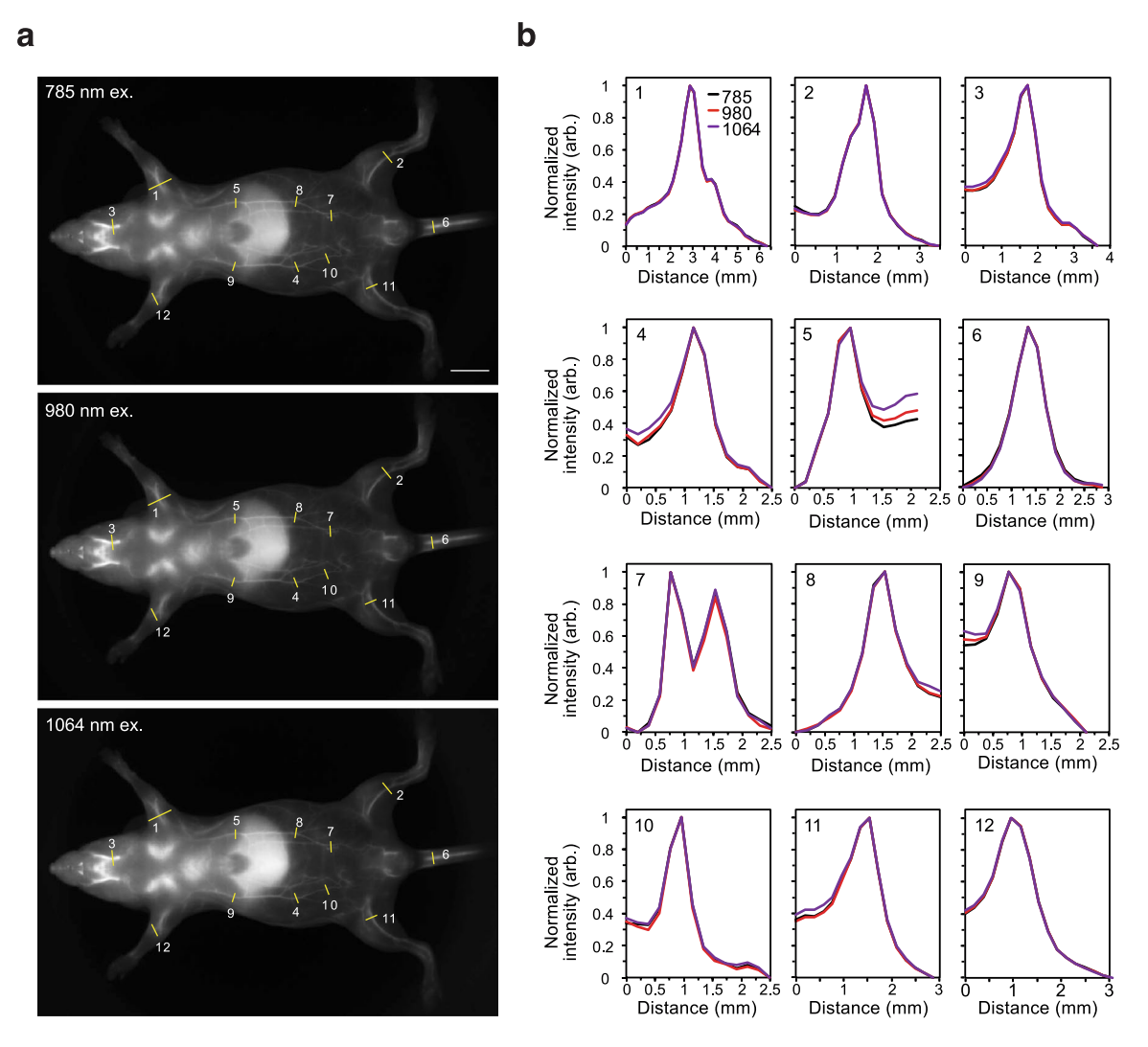
Material presented in this work is included in patent and patent applications US20200140404, EP3634397 and WO2018226720 with authors E.M.S and E.D.C. and PCT/EP2020065753 with authors O.T.B., E.D.C., J.G.P.L., M.W., S.R., M.S. and E.M.S.

Additional information

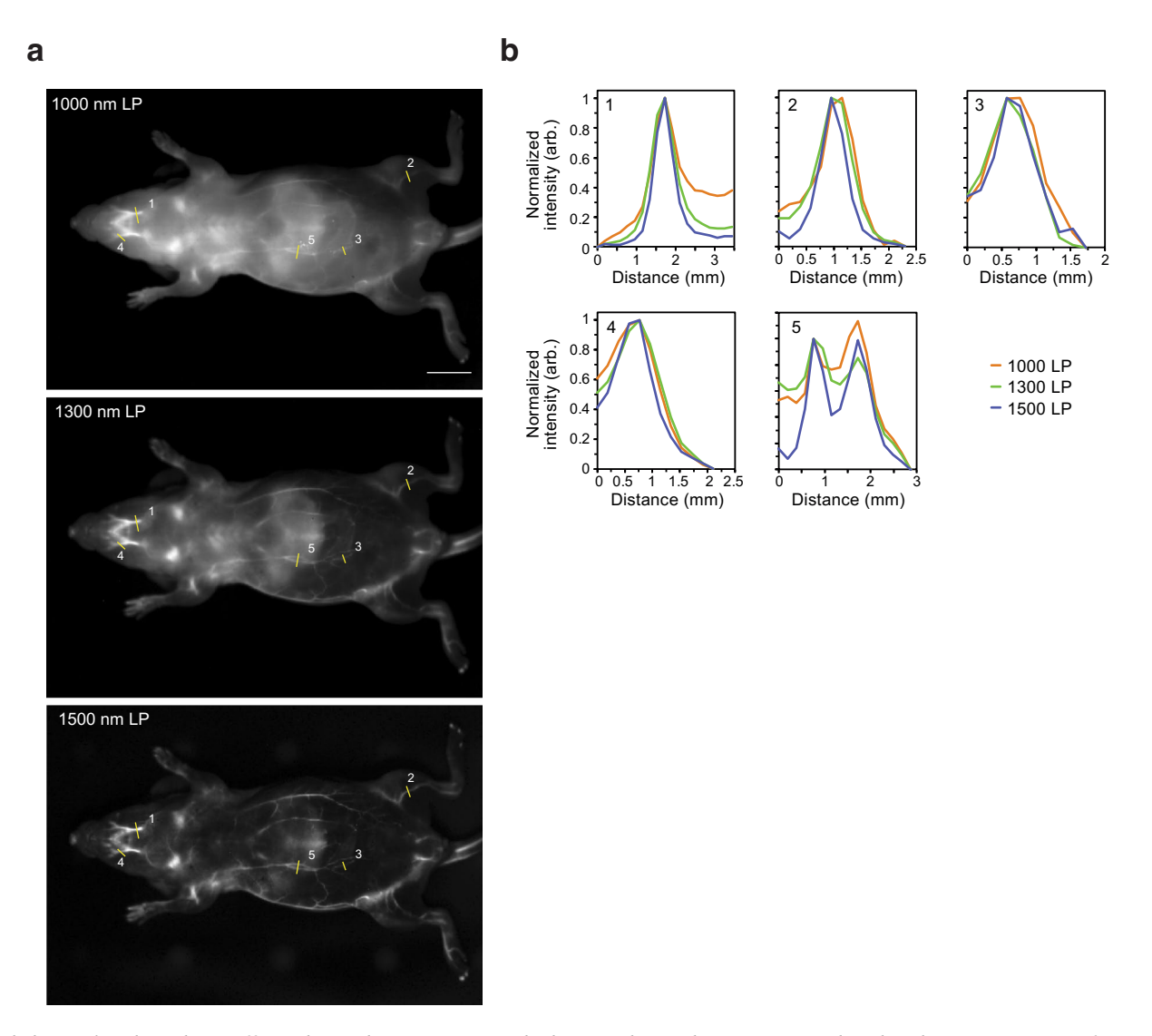
Extended data is available for this paper at https://doi.org/10.1038/s41557-020-00554-5. **Supplementary information** is available for this paper at https://doi.org/10.1038/s41557-020-00554-5.

Correspondence and requests for materials should be addressed to O.T.B. or E.M.S. Reprints and permissions information is available at www.nature.com/reprints.

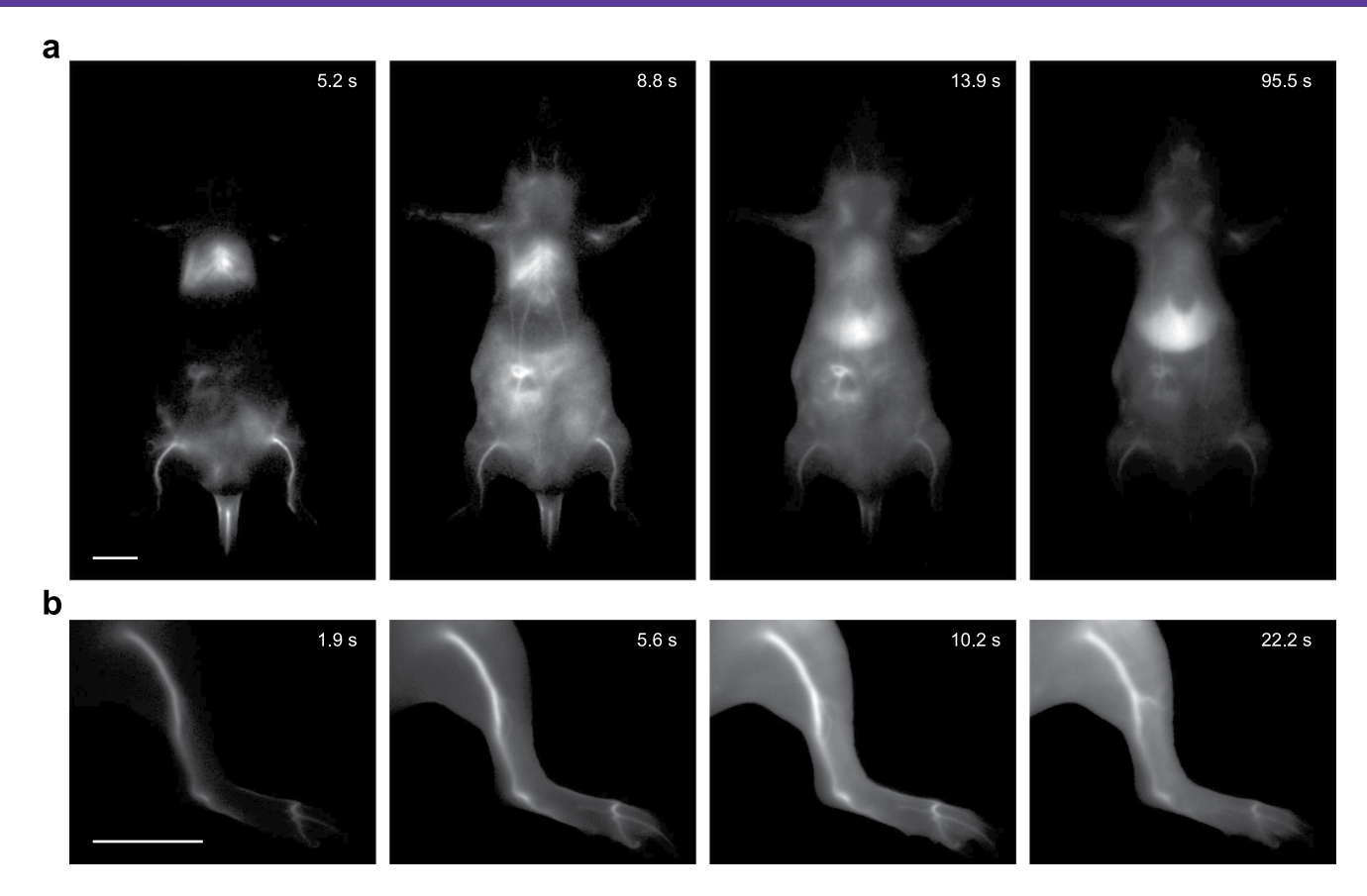
Extended Data Fig. 1 | Retrosynthesis of 7-aminoflavylium heterocycles. The 7-amino-4-methyl flavylium heterocycles were accessed through flavone intermediates **13**. Three routes were used to obtain flavones **13**, Mentzer pyrone synthesis, Buchwald-Hartwig coupling, and acylation. Conditions and yields for each derivative can be found in the listed Supplementary Tables.



Extended Data Fig. 2 | Resolution effects upon excitation multiplexing and single-channel detection in the SWIR. a, Images of a mouse phantom acquired after injection of JuloFlav7 (3) (94 nmol) and immediate euthanasia. Images were acquired with 785 nm excitation (93 mWcm⁻²), 980 nm (30 mWcm⁻²), and 1,064 nm (11 mWcm⁻²) and collection 1,150-1,700 nm (48 ms, 20 fps). Displayed images are averaged over 200 frames. **b**, To observe resolution, 12 cross-sections were drawn over different vessels (labelled in a) and the baseline subtracted and normalized cross-sections are overlaid. ex. = excitation; LP = longpass.



Extended Data Fig. 3 | Resolution effects observed upon emission multiplexing with a single excitation wavelength in the SWIR. a, Images of a mouse phantom acquired after injection of JuloFlav7 (3) (94 nmol) and immediate euthanasia, after one freeze-thaw cycle. Images were acquired with 980 nm excitation. Laser powers and exposure time are as follows (1) 1,000 nm LP = 8.1 mWcm⁻², 30 ms; 1,300 nm LP = 24 mWcm⁻², 500 ms; 1,500 nm LP = 177 mWcm⁻², 500 ms. Displayed images are averaged over 200 frames. **b**, To observe resolution, 5 cross-sections were drawn over different vessels (labelled in a) and the baseline subtracted and normalized cross-sections are overlaid. LP = longpass.



Extended Data Fig. 4 | Imaging with 1064 nm excitation after injection of JuloFlav7 (3) micelles. a, Whole mouse imaging at selected time-points after i.v. injection of JuloFlav7 (3) micelles (44 nmol) in PBS buffer with excitation at 1,064 nm (103 mWcm⁻¹) and 1,150-1,700 nm collection (8 ms exposure time, 100 fps). b, Imaging of the mouse hind-limb at selected time points after i.v. injection of JuloFlav7 (3) micelles (55 nmol) with excitation at 1,064 nm (95 mWcm⁻¹) with 1,100-17,00 nm collection (9 ms exposure time, 100 fps). Displayed images are averaged over 5 frames. Scale bars represent 1 cm. Data are representative of two replicate experiments.

natureresearch

Corresponding author(s): Ellen M. Sletten, Oliver T. Bruns

Last updated by author(s): July 10, 2020

Reporting Summary

Nature Research wishes to improve the reproducibility of the work that we publish. This form provides structure for consistency and transparency in reporting. For further information on Nature Research policies, see <u>Authors & Referees</u> and the <u>Editorial Policy Checklist</u>.

_				٠.	
Ç.	ta:	t۱	IC:	ŀί	CS
J	ıа	u	ادا	ιJ	CO

For	all statistical analys	es, confirm that the following items are present in the figure legend, table legend, main text, or Methods section.			
n/a	Confirmed				
	The exact sam	ple size (n) for each experimental group/condition, given as a discrete number and unit of measurement			
	A statement o	n whether measurements were taken from distinct samples or whether the same sample was measured repeatedly			
	The statistical Only common to	test(s) used AND whether they are one- or two-sided ests should be described solely by name; describe more complex techniques in the Methods section.			
\boxtimes	A description	of all covariates tested			
\boxtimes	A description	of any assumptions or corrections, such as tests of normality and adjustment for multiple comparisons			
	A full descript AND variation	ion of the statistical parameters including central tendency (e.g. means) or other basic estimates (e.g. regression coefficient) (e.g. standard deviation) or associated estimates of uncertainty (e.g. confidence intervals)			
	For null hypothesis testing, the test statistic (e.g. <i>F</i> , <i>t</i> , <i>r</i>) with confidence intervals, effect sizes, degrees of freedom and <i>P</i> value noted Give <i>P</i> values as exact values whenever suitable.				
\boxtimes	For Bayesian analysis, information on the choice of priors and Markov chain Monte Carlo settings				
\boxtimes	For hierarchical and complex designs, identification of the appropriate level for tests and full reporting of outcomes				
\boxtimes	\square Estimates of effect sizes (e.g. Cohen's d , Pearson's r), indicating how they were calculated				
		Our web collection on <u>statistics for biologists</u> contains articles on many of the points above.			
So	ftware and c	ode			
Poli	cy information abou	ut <u>availability of computer code</u>			
Da	ata collection	Image data collection was facilitated by a semi-automatic imaging algorithm using MATLAB (MathWorks, 2017a and 2019a) and Arduino Integrated Development Environment (v. 1.8.7). The acquisition code will be made available at GitHub. Flow cytometry data was collected using CellQuest (BD Bioscience, version 3.3)			

11.0.3-18688) or TopSpin (Bruker, 4.0.6). Flow cytometry data was processed with FlowJo (BD Biosciences, v10).

For manuscripts utilizing custom algorithms or software that are central to the research but not yet described in published literature, software must be made available to editors/reviewers. We strongly encourage code deposition in a community repository (e.g. GitHub). See the Nature Research guidelines for submitting code & software for further information.

Images were processed using the Fiji distribution of Imagej (1.52p), or with Python 3, using the libraries scikit-image for image

processing, NumPy for array manipulations, and Matplotlib for plotting. NMR data was processed with MestReNova (Mestrelab research,

Data

Data analysis

Policy information about availability of data

All manuscripts must include a data availability statement. This statement should provide the following information, where applicable:

- Accession codes, unique identifiers, or web links for publicly available datasets
- A list of figures that have associated raw data
- A description of any restrictions on data availability

Image data sets, including all raw and processed imaging data generated in this work will be made available at BioImage Archive (EMBL-EBI). All other datasets that support the findings of this study are contained within the manuscript and its Supplementary Information.

Field-spe	ecific re	eporting		
Please select the or	ne below that	is the best fit for your research. If you are not sure, read the appropriate sections before making your selection.		
∑ Life sciences		Behavioural & social sciences		
For a reference copy of t	the document wit	th all sections, see <u>nature.com/documents/nr-reporting-summary-flat.pdf</u>		
Life scier	nces st	udy design		
All studies must dis	sclose on thes	e points even when the disclosure is negative.		
Sample size	As the nature of the experiments were exploratory, no sample-size calculation was performed. The number of individuals in each experiment was determined to validate technological advance and was not used to validate a biological hypothesis.			
Data exclusions	None.	e.		
Replication	The multiplexing imaging technique was replicated in five different mice and all replication attempts were successful. Three color imaging and two-color visualization of lymphatic and circulatory function were each performed in two mice. Awake animal imaging, liver clearance, and necropsy, as a natural extension of the same technology and to further replicate/validate the technology, were each performed once. Fast single-color imaging was performed in two mice. Two separate cell viability experiments were performed.			
Randomization	Randomizatio	on was not relevant to the study as distinct groups were not allocated.		
Blinding	Investigators	were not blinded as a biological hypothesis was not tested.		
We require informatic system or method list Materials & exp n/a Involved in th Antibodies Eukaryotic Palaeontol Animals an	perimental ne study cell lines ogy d other organis search participa	n/a Involved in the study ChIP-seq Flow cytometry MRI-based neuroimaging		
Policy information about <u>cell lines</u> Cell line source(s)		HEK-293 cells (ATCC CRL-1573) were sourced from ATCC.		
Authentication		After purchase from ATCC, cell line was not further authenticated.		
Mycoplasma contamination		The cell line tested negative for mycoplasma contamination.		
Commonly misidentified lines (See ICLAC register)		N/A		
Animals and	other or	ganisms		
Policy information	about <u>studies</u>	<u>involving animals</u> ; <u>ARRIVE guidelines</u> recommended for reporting animal research		
Laboratory anima	Experiments were performed on athymic nude mice, female, 6-16 weeks old. Mice were housed at 24 °C , 45–65% humidity, with a 12/12 hour light/dark cycle.			
Wild animals The study did not involve wild animals.		The study did not involve wild animals.		

The study did not involve samples collected from the field.

Field-collected samples

Ethics oversight

All ethics and protocols are in accordance with regulations of the government of Upper Bavaria.

Note that full information on the approval of the study protocol must also be provided in the manuscript.

Flow Cytometry

Plots

Confirm that:

- The axis labels state the marker and fluorochrome used (e.g. CD4-FITC).
- The axis scales are clearly visible. Include numbers along axes only for bottom left plot of group (a 'group' is an analysis of identical markers).
- All plots are contour plots with outliers or pseudocolor plots.
- A numerical value for number of cells or percentage (with statistics) is provided.

Methodology

Sample preparation

HEK293 cells (ATCC CRL-1573, sourced from ATCC) in MEM supplemented with fetal bovine serum (FBS), Pen/Strep, and sodium pyruvate were incubated with micelles for 3 hours as stated in Supplementary Fig. 6. The cells were then washed with FACS buffer and incubated on ice with propidium iodide for 15 min.

Instrument

2- Laser BD FACSCalibur Flow Cytometer (BD Biosciences)

Software

Flow cytometry data was collected with CellQuest (BD Bioscience , version 3.3) and analyzed by FlowJo (BD Biosciences, v10)

Cell population abundance

All events were collected and analyzed. No post-sorting was performed.

Gating strategy

A preliminary FSC/SSC gate was implemented on the starting cell population to omit cell debris. PI staining and laser power was adjusted such that there was at least an order of magnitude difference between stained and unstained samples, verified by healthy cells and a heat-kill control.

| Tick this box to confirm that a figure exemplifying the gating strategy is provided in the Supplementary Information.